

# Joint Physics-Based and Data-Driven Time-Lapse Seismic Inversion: Mitigating Data Scarcity

Yanhua Liu, Shihang Feng, Ilya Tsvankin, David Alumbaugh, and Youzuo Lin

*Earth and Environmental Sciences Division, Los Alamos National Laboratory*

*Center for Wave Phenomena, Colorado School of Mines*

*Earth and Environmental Sciences, Lawrence Berkeley National Laboratory*

*email liuyanhua@mines.edu*

## ABSTRACT

In carbon capture and sequestration (CCS), developing rapid and effective imaging techniques is crucial for real-time monitoring of the spatial and temporal dynamics of CO<sub>2</sub> propagation during/after injection. With continuing improvements in computational power and data storage, data-driven techniques based on machine learning (ML) have been effectively applied to seismic inverse problems. In particular, ML helps alleviate the ill-posedness and high computational cost of full-waveform inversion (FWI). However, such data-driven inversion techniques require massive high-quality training data sets to ensure prediction accuracy, which hinders their application to time-lapse monitoring of CO<sub>2</sub> sequestration. We propose an efficient “hybrid” time-lapse workflow that combines physics-based FWI and data-driven ML inversion. The scarcity of the available training data is addressed by developing a new data-generation technique with physics constraints. The method is validated on a synthetic CO<sub>2</sub>-sequestration model based on the Kimberlina storage reservoir in California. The proposed approach is shown to synthesize a large volume of high-quality, physically realistic training data, which is critically important in accurately characterizing the CO<sub>2</sub> movement in the reservoir. The developed hybrid methodology can also simultaneously predict the variations in velocity and saturation and achieve high spatial resolution in the presence of realistic noise in the data.

**Key words:** Time-lapse seismic, data-driven neural network, data scarcity, full waveform inversion

## 1 INTRODUCTION

The importance of CO<sub>2</sub> sequestration has increased in the past decade due to the global warming caused by greenhouse gases. Rapidly imaging and monitoring the spatial and temporal dynamics of CO<sub>2</sub> migration ensures that the supercritical CO<sub>2</sub> is injected at the correct location and does not leak out of the reservoir (e.g., Lumley, 2010; Pevzner et al., 2017). Time-lapse seismic can represent an effective tool for monitoring CO<sub>2</sub> injected into an aquifer (Zhang et al., 2012; Ajo-Franklin et al., 2013; Raknes et al., 2015; Furre et al., 2017; Pevzner et al., 2017).

Full-waveform inversion (FWI) of seismic data has been widely utilized for velocity analysis and, under favorable circumstances, reservoir characterization (Vigh et al., 2014; Asnaashari et al., 2015; Fabien-Ouellet et al., 2017; Singh et al., 2018). FWI can potentially provide estimates of the time-lapse parameter variations with high spatial resolution. Time-lapse FWI (TLFWI) strategies proposed for monitoring hydrocarbon production and CO<sub>2</sub> injection (Quei er and Singh, 2013; Asnaashari et al., 2015; Liu and Tsvankin, 2021) include the parallel-difference, sequential-difference, and double-difference techniques. The parallel-difference method (Plessix et al., 2010) uses the same initial model for the baseline and monitor inversions, whereas the sequential-difference method (Asnaashari et al., 2012) inverts the baseline data to build the initial model for the monitor inversion. The double-difference technique (Watanabe et al., 2004; Denli and Huang, 2009; Lin and Huang, 2015) estimates the time-lapse parameter variations by inverting the difference between the monitor and baseline data sets. Liu and Tsvankin (2021, 2022) extend these

time-lapse FWI techniques to realistic elastic anisotropic media. Huang and Zhu (2020) implement uncertainty estimation to the acoustic time-lapse FWI results.

However, FWI suffers from ill-posedness, cycle-skipping, and high computational cost because of the nonlinearity of the inverse problem (Virieux and Operto, 2009; Liu et al., 2013; Feng and Schuster, 2019; Wu and Lin, 2019; Zhang and Alkhalifah, 2020; Feng et al., 2021; Zhang and Gao, 2021). In addition, FWI cannot directly estimate the CO<sub>2</sub> saturation, though empirical and statistical petrophysics relationships have to be employed as a post inversion step to reconstruct the saturation distribution from the inverted velocity field (Grana and Rossa, 2010; Ali and Al-Shuhail, 2018).

Recently, with the increased computational power and the revitalization of deep neural networks, significant research and development efforts have been put into data-driven ML methods for seismic imaging (Hale, 2013; Dahlke et al., 2016; ArayaPolo et al., 2017; Cao and Roy, 2017; Yuan et al., 2019; Li et al., 2021). Such methods aim to approximate the inversion operator by neural networks based on the universal approximation theorem (Zhang and Lin, 2020). Data-driven techniques can potentially produce a more accurate reconstruction of subsurface structure than physics-based FWI in a significantly shorter time, which is essential for real-time monitoring.

However, the accuracy of data-driven inversion depends on the generalization ability of the employed networks and the quality and volume of the available training data (Zhang and Alkhalifah, 2020; Yang et al., 2021; Zhang and Gao, 2021). The generalization ability refers to the performance of a network on testing data sets that are significantly different from the training data. Considering that the medium outside the reservoir does not substantially change during injection, the distribution shift between the testing monitor data and the training data should not be a significant issue in time-lapse monitoring.

However, obtaining high-quality training data can be challenging for typical CO<sub>2</sub> sequestration projects. To address this data scarcity problem, Renán et al. (2022) develop an active learning strategy by incorporating the wave equation to expand the training data set. Yang et al. (2021) present a convolutional neural network to augment training data using such physics information as the wave equation and time-lapse variations of P-wave velocity. Despite some encouraging results, these two methods still require extensive training data in advance, which limits their applicability. Yuan et al. (2019) randomly perturb the inverted baseline model of the reservoir produced by physics-based FWI to generate training data that can be used to predict the time-lapse velocity changes. However, because the data generation is random, the training data set can be physically unrealistic and results in incorrect predictions.

We begin by discussing the methodology of physics-based and data-driven inversions and then outline their application to time-lapse seismic data. To overcome the aforementioned issues related to data scarcity, we propose a “hybrid” time-lapse strategy that combines physics-based FWI with data-driven inversion (called “InvNet-VelSat”). The developed data-generation algorithm simulates high-quality velocity and saturation training models utilizing the available physics information and prior knowledge (i.e., the inverted baseline model and well logs). The data-generation method and the proposed hybrid approach are tested on the Kimberlina reservoir model, assuming that only the baseline and one monitor data set are available. The reconstructed time-lapse variations are compared with those produced by the pure physics-based and data-driven techniques. The generalization ability and robustness of our algorithm is validated by applying it to other monitor surveys and noisy seismic data. Finally, we discuss the impact of the prior information and the quality of the simulated training data on the reconstructed time-lapse variations.

## 2 REVIEW OF PHYSICS-BASED AND DATA-DRIVEN INVERSIONS

### 2.1 Physics-based full-waveform inversion

Full-waveform inversion iteratively minimizes the difference between the observed and simulated data in the process of updating the subsurface model. Acoustic models may represent a suitable first-order approximation for CO<sub>2</sub> monitoring because shear-wave velocity is not expected to be influenced by supercritical CO<sub>2</sub> (Mavko and Mukerji, 1998; Carcione et al., 2006; Queiβer and Singh, 2010). For acoustic isotropic media, FWI operates with shot gathers of the observed ( $\mathbf{p}^{\text{obs}}$ ) and simulated ( $\mathbf{p}^{\text{sim}}$ ) pressure field.

The L<sub>2</sub>-norm FWI objective function  $S(\mathbf{m})$  is then defined as (e.g., Tarantola, 1984):

$$S(\mathbf{m}) = \frac{1}{2} \left\| \mathbf{p}^{\text{sim}}(\mathbf{m}) - \mathbf{p}^{\text{obs}} \right\|^2, \quad (1)$$

where  $\mathbf{m}$  includes the gridded P-wave velocity and density models.

Due to the high nonlinearity of FWI, the model-updating procedure can be trapped in local minima. Therefore, the initial model needs to be in the basin of convergence near the global minimum.

The acoustic wave equation used here to simulate seismic data has the form:

$$\frac{1}{V_p^2(\mathbf{x})} \frac{\partial^2 p(\mathbf{x}, t; \mathbf{x}_s)}{\partial t^2} - \nabla^2 p(\mathbf{x}, t; \mathbf{x}_s) = \delta(\mathbf{x} - \mathbf{x}_s) f(t), \quad (2)$$

where  $V_p$  is the P-wave velocity,  $p$  is pressure wavefield,  $f(t)$  is the source signal, “ $\nabla^2$ ” denotes the Laplacian operator, and  $\mathbf{x}_s$  and  $\mathbf{x}$  are the source and receiver locations, respectively. The gradient of the objective function with respect to the model parameters is computed from the adjoint-state method. A nonlinear conjugate-gradient algorithm is employed for updating the velocity:

$$V_p^{k+1} = V_p^k - \alpha_k \nabla S(V_p^k), \quad (3)$$

where  $\alpha_k$  is the step length at the  $k$ th iteration.

## 2.2 Data-driven InvNet-VelSat

In contrast to physics-based FWI methods, data-driven inversion aims to form a pseudoinverse operator  $F$ , which performs mapping from the input to the model (target) domain (i.e., from the shot gathers  $\mathbf{p}$  to the medium parameters  $\mathbf{m}$ )

$$\mathbf{m} \approx F(\mathbf{p}). \quad (4)$$

The universal approximation theorem (Hornik et al., 1990) allows the neural network to approximate most complex functions given sufficient training data. In particular, InversionNet is an end-to-end convolutional neural network (CNN) developed by Wu and Lin (2019) and based on the above theorem. The input is the recorded pressure and the output is the P-wave velocity model. The CNN consists of an encoder and a decoder. The encoder contains five convolution blocks followed by maximum pooling to extract high-level features (representing the input) from the pressure data and significantly reduce the data dimension. Each convolution block includes a convolution layer, batch normalization, and a LeakyReLU activation function. The decoder, which comprises five deconvolution blocks, translates these features into the velocity model.

Since saturation is closely related to CO<sub>2</sub> diffusion in the subsurface, we propose a modified network (InvNet-VelSat, Figure 1) to simultaneously predict both velocity and CO<sub>2</sub> saturation. The structures of the encoder and decoder for the velocity prediction in InversionNet are incorporated into InvNet-VelSat. The decoder added for predicting the saturation is parallel to that for the velocity prediction. The Mean Absolute Error (MAE) is employed to measure the training and testing loss and to preserve sharp boundaries in the predicted models.

## 3 METHODOLOGY OF TIME-LAPSE PROCESSING

The difference between the medium parameters reconstructed from the monitor and baseline surveys reflects the temporal changes in the subsurface properties caused by the injected CO<sub>2</sub>. Next, we discuss three different time-lapse strategies involving physics-based FWI and data-driven InvNet-VelSat.

### 3.1 Strategy 1: Physics-based time-lapse FWI

In time-lapse FWI based on the parallel-difference method (Plessix et al., 2010), the baseline seismic data are inverted starting from a certain initial model. The same initial model is then used in the monitor inversion. The parameter changes are calculated by subtracting the inverted baseline parameters from those of the monitor model.

### 3.2 Strategy 2: Data-driven time-lapse inversion

The data-driven algorithm uses the InvNet-VelSat for the monitor inversion. The network is first trained on extensive pre-existing training data set including the baseline survey. Once fully trained, InvNet-VelSat predicts both velocity and saturation from the observed monitor data. Since the baseline models are assumed to be known in advance, the time-lapse variations represent the difference between the predicted monitor and the actual baseline parameters.

InvNet-VelSat has several advantages over FWI. First, FWI suffers from cycle-skipping (convergence) problems caused by local minima of the objective function (e.g., Virieux and Operto, 2009). Mitigating cycle skipping requires a sufficiently accurate initial model that is not always available. Second, FWI is computationally expensive (Virieux and Operto, 2009; Wu and Lin, 2019), while well-trained InvNet-VelSat can predict the subsurface properties with sufficient resolution in seconds. The high efficiency of InvNet-VelSat is especially important in real-time monitoring during oil/gas production and CO<sub>2</sub> sequestration.

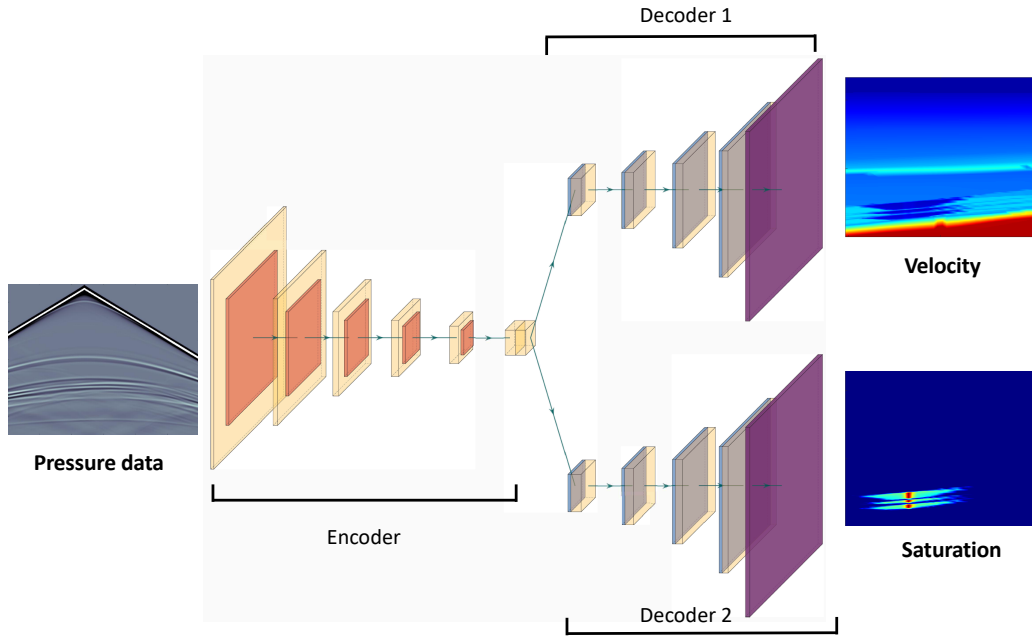


**Figure 1.** Network architecture of InvNet-VelSat. The encoder, built with five convolution layers and maximum pooling, extracts high-level features from the input seismic data to the latent space and reduces the dimensions of the feature map. Each of the two decoders consists of five deconvolution layers and translates the latent variable to the velocity (output 1) and saturation (output 2) models.

Furthermore, InvNet-VelSat can simultaneously predict velocity and saturation, while FWI has to convert the reconstructed velocity field into saturation via empirical petrophysics equations Xue et al. (2009). In addition, the background model stays almost unchanged outside the reservoirs, which mitigates the generalization issue in applying InvNet-VelSat to time-lapse processing. Although the velocity model can be dramatically altered at the near surface where seasonal changes and precipitation can dramatically alter the near surface velocity structure, it is outside the scope of this work and needs additional investigation. However, all data-driven inversions, including InvNet-VelSat, assume that a large amount of high-quality data (i.e., sufficiently similar to the testing data) is available for training purposes.

### 3.3 Strategy 3: Hybrid approach

The proposed hybrid approach (Figure 2), which combines the physics-based and data-driven methods, does not require pre-existing training data. First, we apply FWI to the baseline survey to reconstruct the baseline velocity model. For real-time monitoring of CO<sub>2</sub> sequestration, we process the monitor survey with InvNet-VelSat. To generate a sufficient volume of high-quality training data, the inverted baseline velocity is perturbed in the CO<sub>2</sub> reservoir, whereas the rest of velocity model remains unchanged. Hence, the prediction capability of InvNet-VelSat largely depends on the accuracy of the inverted baseline model, which is used to generate the training data. Our method is described in more detail below.

#### 3.3.1 Velocity-generation method

We employ the following prior knowledge when generating synthetic velocity models (Figure 3).

1. The subsurface structure before the injection is obtained from physics-based FWI, which is assumed to provide sufficient spatial resolution. The reconstructed baseline velocity model is changed only inside the reservoir to obtain the training velocity models for the model prediction from the monitor data.

2. CO<sub>2</sub> migration in the reservoir obeys certain laws of physics. Because supercritical CO<sub>2</sub> is less dense than water, the injected CO<sub>2</sub> should first accumulate near the top of the reservoir and then diffuse along the reservoir boundary.

3. Well logs (i.e., sonic, saturation, density, and electrical resistivity) from the injection and monitor wells are used to provide geologic and geophysical information, and thus constrain the inversion process.

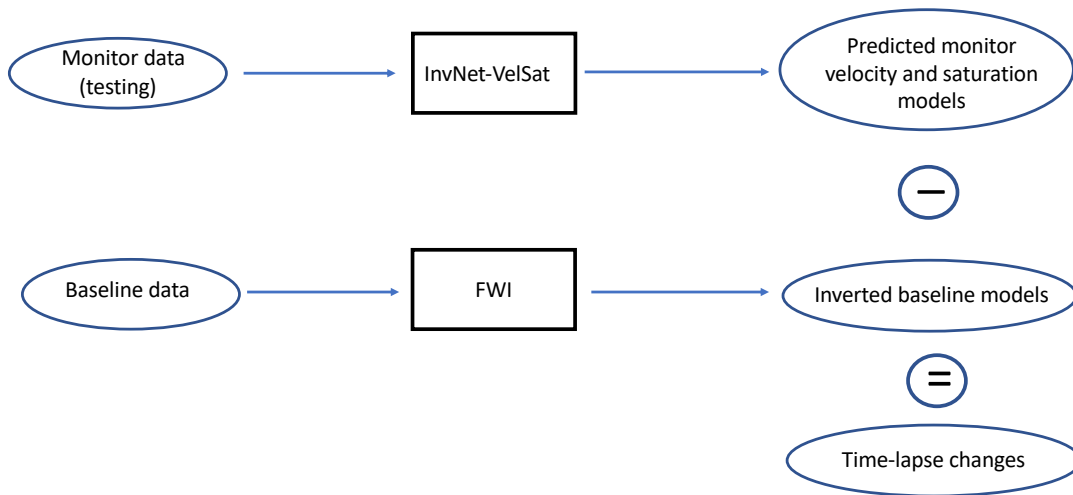


**Figure 2.** Workflow of the hybrid time-lapse strategy that combines physics-based FWI and data-driven InvNet-VelSat. FWI is employed to invert the baseline data and obtain the background velocity distribution for generating synthetic training samples. The trained InvNet-VelSat is applied to the monitor survey to predict both the velocity and saturation models. The temporal velocity changes are computed by subtracting the inverted baseline velocity model from the predicted monitor model.

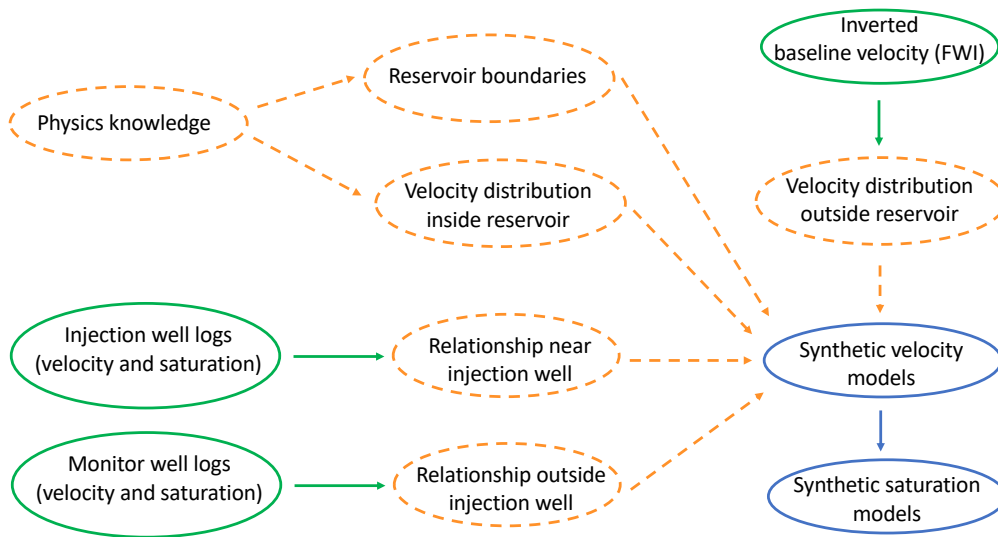


**Figure 3.** Workflow of the velocity- and saturation-simulation algorithms. The dashed orange oval marks the prior information and the empirical relationship between the velocity and saturation obtained from well logs. The solid green oval marks the inverted baseline velocity field used for generating training velocity models, and the sonic and saturation logs used for obtaining saturation. The solid blue oval marks the synthetic velocity and saturation models generated for training.

The physics-related information used in our data-generation method typically can be obtained in practice. Therefore, the proposed hybrid approach and data-generation algorithm should be applicable to time-lapse field data.

### 3.3.2 Synthetic CO<sub>2</sub>-saturation models

Although the relationship between P-wave velocity and CO<sub>2</sub> saturation can be inferred from empirical equations based on laboratory and field experiments (Gassmann, 1951; Mavko and Mukerji, 1995), this approach relies on the geologic similarity between

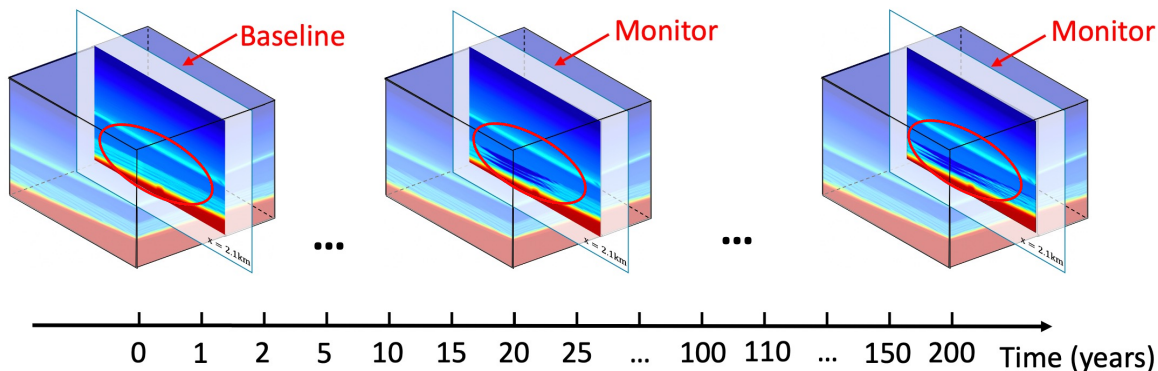


**Figure 4.** Visualization of the actual 4D velocity model. The baseline and monitor surveys are simulated for the same 2D vertical profiles before and during (or after) CO<sub>2</sub> injection. The time-lapse changes are encircled in red.

the field of interest and those used to derive the equations. Here, we obtain the relationship between velocity and saturation from the available well logs using linear fitting equations (Figure 3).

Because the saturation level in the vicinity of the injection well is higher than that near the monitor wells, we separate the reservoir into two parts — the injection zone and the monitor zone. The velocity-saturation plots from the Kimberlina well logs indicate a linear relationship between these two parameters, but the slope changes between the low- and high-saturation parts. Therefore, we approximate the saturation-velocity relationship with two linear functions based on the saturation level.

## 4 SYNTHETIC EXAMPLES

### 4.1 Kimberlina data set

The physics-based, data-driven, and hybrid strategies are applied to monitor and predict CO<sub>2</sub> migration using a synthetic data set. (We have been unable so far to find publicly available field data suitable for our purposes.) The test is performed on the 4D Kimberlina reservoir data generated by several institutions (Alumbaugh et al., 2021) as part of the U.S. Department of Energy “SMART Initiative” (U.S. Department of Energy, 2019). This data set is generated from multiple CO<sub>2</sub> injection reservoir simulations for a model similar to the geologic structure of a commercial-scale carbon-sequestration reservoir at the Kimberlina site in the southern San Joaquin Basin (Wagoner, 2009). The Kimberlina time-lapse data can be used to evaluate the effectiveness and robustness of different geophysical techniques for monitoring CO<sub>2</sub> migration.

The data include 29 3D P-wave velocity and CO<sub>2</sub>-saturation models simulated for over 200 years with a grid size of  $10 \times 10 \times 10$  m ( $601 \times 601 \times 351$  points; Figure 4). We slice each 3D model along the  $y$ -axis with a spatial interval of 100 m starting from  $x = 0$  to obtain 53 2D samples, which yields 1,537 velocity and saturation models (referred to as the “actual data”). In addition, time-lapse multiphysics well logs have been synthesized for four hypothetical well locations (Figure 5). These CO<sub>2</sub>-saturation, density, sonic velocity, and resistivity logs are available for 0, 1, 2, 5, 10, 15, and 20 years after the start of the CO<sub>2</sub> injection. Note that these four wells are not confined to the same vertical plane.

The 2D slice containing the injection well in year 0 (i.e., before the injection) is treated as the baseline model. The monitor data are acquired in the same 2D vertical plane to map the movement of the injected CO<sub>2</sub> and compute the time-lapse parameter variations. The temporal velocity changes (Figure 5) are heterogeneous and vary between  $x = -0.5$  km and  $x = 0$ . The saturation changes in the reservoir are also heterogeneous and vary between zero and unity. Both velocity and saturation models have a grid size of  $10 \times 10$  m.

There are three important geologic structures in the velocity model (Figure 5): the low-velocity layer immediately above the reservoir region (Zone 1), the three reservoirs themselves (Zone 2), and the high-velocity dipping layer beneath the reservoirs (Zone 3). Note that the shallow low-velocity horizon is not a water layer.

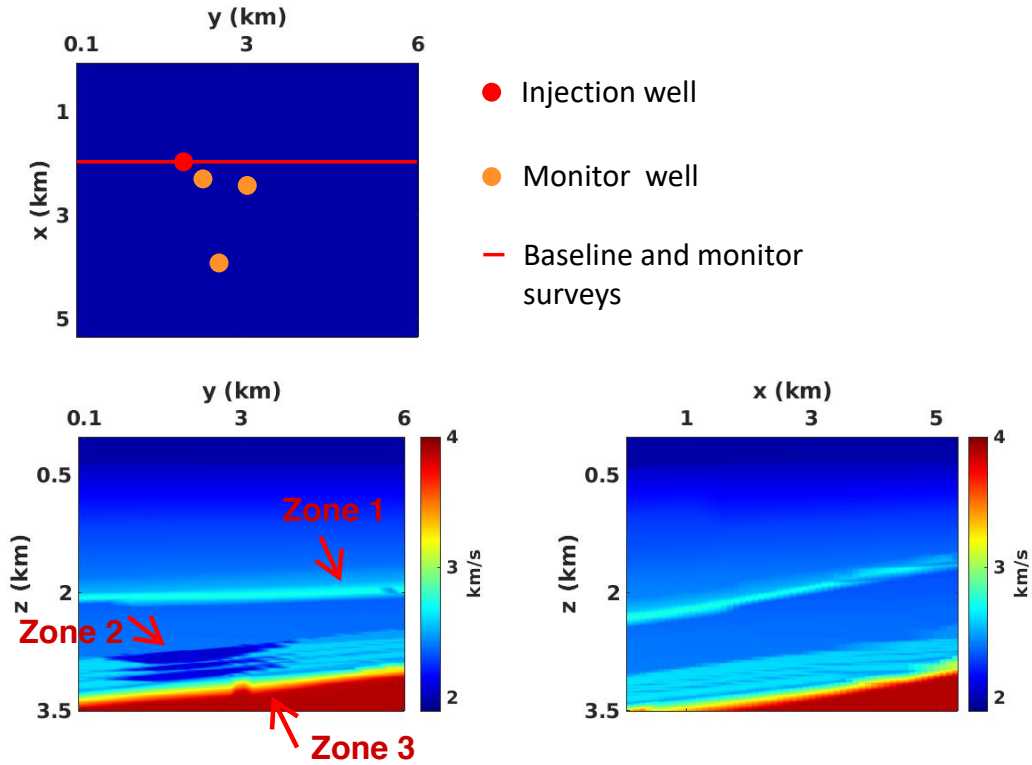


**Figure 5.** 3D geometry of the Kimberlina data set. The injection well and three monitor wells are denoted by the red and orange dots, respectively, in the  $[x, y]$ -plane. The red line in the  $[x, y]$ -plane shows the projection of the baseline and monitor surveys. The red arrows in the  $[y, z]$ -plane point to three structures used for evaluating the effectiveness of time-lapse strategies: the low velocity layer above the reservoirs (Zone 1), the three  $\text{CO}_2$  reservoirs (Zone 2), and the high-velocity dipping layer below the reservoirs (Zone 3).

#### 4.2 Physics-based time-lapse FWI

The synthetic acoustic wavefield is excited by 37 shots (point explosions) placed with a constant increment (80 m) along a horizontal line at a depth of 10 m. The source signal is the Ricker wavelet with a central frequency of 10 Hz. We employ 294 receivers evenly distributed with an increment of 20 m along the horizontal line 20 m deep. The initial baseline and monitor models are identical (Figures 7a and 7b) and computed by Gaussian smoothing of the actual baseline velocity field (Figure 6a) with a standard deviation of 15. Note that the  $\text{CO}_2$  plumes are not present in the initial model. FWI is applied to the simulated pressure recordings using a multiscale approach with four frequency bands starting from 2 Hz (2-5, 2-8, 2-13, 2-20 Hz; Singh et al., 2020; Liu and Tsvankin, 2021).

Figures 7d and 7e show that FWI reconstructs the baseline and monitor velocity distribution with sufficient accuracy. Particularly, the “bump” in Zone 3 and the low-velocity region in Zone 1 (Figures 7d and 7e) are well resolved in both the baseline and monitor models. There are inversion errors (Figures 7f) at depth, especially near the  $\text{CO}_2$  plumes because the monitor inversion, which starts from the initial baseline model, could not adequately resolve the reservoirs. In addition, there are errors at the reservoir boundaries (i.e., in the thin nonpermeable layers) caused primarily by edge (smoothing) artifacts in the  $L_2$ -norm objective function (Schmidt, 2005; Zhang and Zhang, 2012).

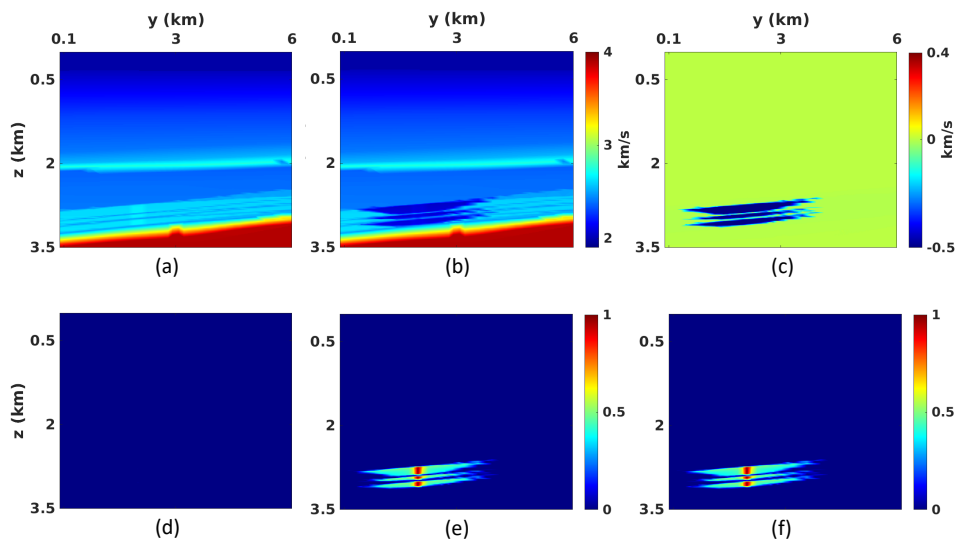


**Figure 6.** P-wave velocity of the (a) baseline Kimberlina model and (b) monitor model in year 20 with a grid size of  $10 \times 10$  m.  $\text{CO}_2$  saturation for the (d) baseline and (e) monitor model in year 20. The actual time-lapse changes of the (c) P-wave velocity and (f) saturation.

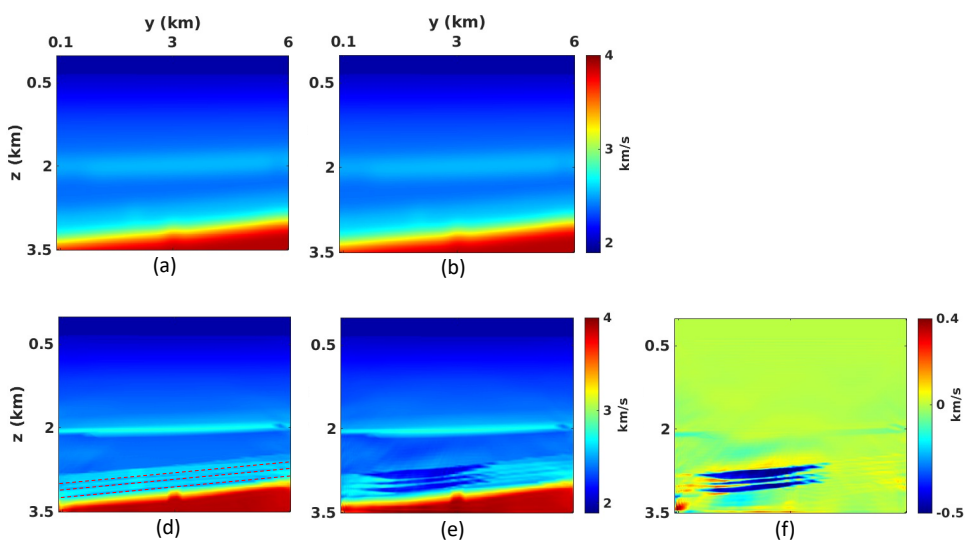


**Figure 7.** Initial P-wave velocity for the inversion of the (c) baseline and (d) monitor data. P-wave velocity obtained by the physics-based FWI: (d) baseline velocity, (e) monitor velocity, and (f) time-lapse velocity variations. The dashed red lines on plot (d) mark the reservoir boundaries.

### 4.3 Data-driven time-lapse inversion

The data-driven strategy assumes that the entire Kimberlina data set (1,537 velocity and saturation samples) is available. The seismic data are simulated using the same survey configuration as in the previous physics-based FWI test. The monitor survey in year 20 provides the testing data. The remaining actual data for over 200 years are randomly divided into the training (1,436 samples) and validation (100 samples) sets. The loss of the training test converges at around 0.05 after 2,212 epochs. Then the testing monitor data are inverted by the trained network.

Figure 8 shows that both the velocity and saturation for the monitor survey are generally predicted with acceptable accuracy. However, the shallow low-velocity layer, the low-velocity anomaly in Zone 1, and the small “bump” in Zone 3 are not well reconstructed either due to the limitations of the training data set. Specifically, the 3D Kimberlina model is laterally heterogeneous, and the 2D velocity distribution varies for different vertical profiles. Only a relatively small fraction of the velocity models contains

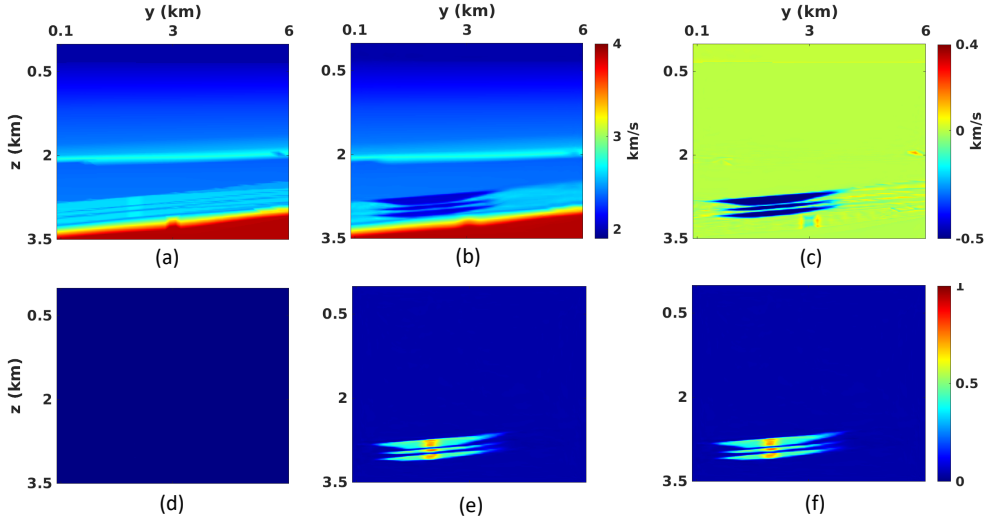


**Figure 8.** Actual baseline (a) velocity and (d) saturation models. The monitor (b) velocity and (e) saturation models predicted by the data-driven time-lapse inversion. The time-lapse variations of (c) velocity and (f) saturation.

such geologic features as the “bump.” Thus, it is challenging for InvNet-VelSat to capture those features in the training data and predict them from the monitor samples.

Those limitations of the training data lead to errors in the background saturation model (Figures 8e and 8f), which deviates from the actual saturation changes (Figures 6f). In addition, the saturation near the injection well is underestimated, which can be explained by the insensitivity of seismic acoustic velocity to high CO<sub>2</sub> saturation (Xue et al., 2009; Kim et al., 2010) and again the incompleteness of the training data.

#### 4.4 Hybrid strategy

According to the proposed hybrid strategy, FWI is first employed to reconstruct the baseline model (Figure 7d). To obtain synthetic velocity models, we first identify three aquifer layers and their top and bottom boundaries from the recovered baseline velocity (Figure 7d) and well logs. We then keep the velocity outside these layers unchanged because the temporal and spatial velocity variations are assumed to be confined to the reservoirs. Well logs provide the velocity profiles in the wells. We identify the maximum and minimum velocity values in the reservoirs for all years from sonic well logs. The velocity in the reservoirs is perturbed within that range for generating a large number of velocity models. After obtaining the training velocity models, linear fitting equations are employed to build the relationship between the velocity and saturation at the injection well using the available well logs. The velocity-saturation relationship away from the injection well is found from linear fitting equations using the monitor-well logs. Note that these relationships may not be applicable to other data sets.

Reservoir simulation, required to accurately model the shape of CO<sub>2</sub> plumes, involves such parameters as permeability and viscosity, which are not available to us. Therefore, we approximate CO<sub>2</sub> movement in the aquifer layers by defining a transportation velocity function. According to this function, CO<sub>2</sub> moves parallel to the upper reservoir boundary with a speed that exponentially decreases with depth. Hence, buoyancy-driven CO<sub>2</sub> moves faster in the upper reservoir (Sigfusson et al., 2015):

$$V_c^d = V_c^{d_0} e^{-c(d-d_0)}, \quad (5)$$

where  $V_c^d$  is the velocity of CO<sub>2</sub> migration at depth  $d$ ,  $d_0$  is the depth of the reservoir top boundary, and  $c$  is a constant that controls the rate of decrease of  $V_c^d$ . Note that the transportation function is based on the structure of the Kimberlina reservoir and, therefore, may need to be modified for other data sets.

The well logs show that the P-wave velocity in the plumes varies between 1.9 km/s and 2.5 km/s. To simplify the velocity distribution, we ignore its lateral variation between the wells. A total of 28,000 training data samples are generated for different velocities ranging from 2.0 km/s to 2.3 km/s with an increment of 0.1 km/s.

Comparison with the actual velocity models (Figures 9a-9d) demonstrates that the synthetic velocity samples (Figures 9e-9h) are physically realistic and capture the spatial and temporal dynamics of CO<sub>2</sub> migration inside the reservoirs. However, the contours

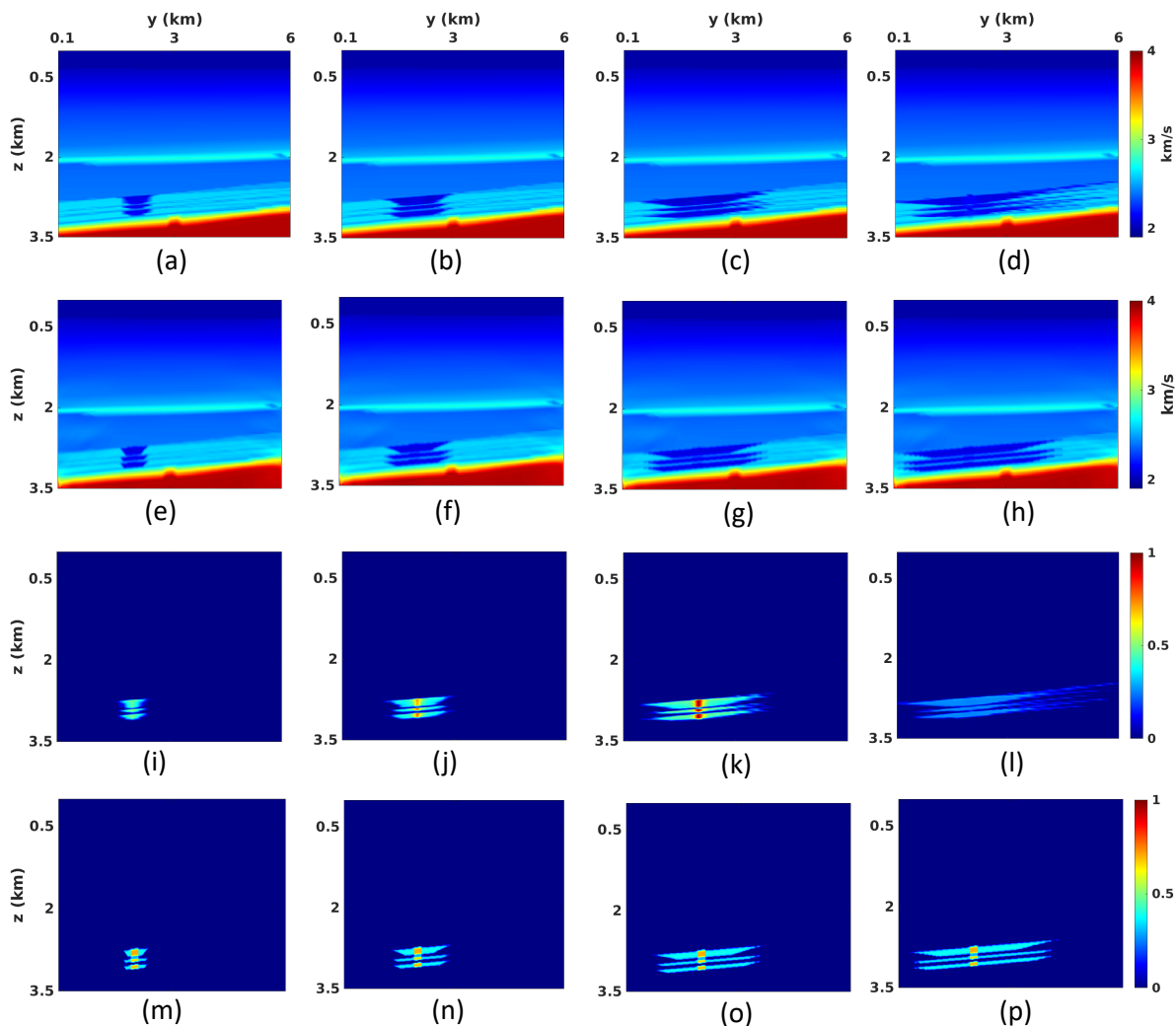


**Figure 9.** Actual P-wave velocity model (first row) in (a) year 1 (b) year 5, (c) year 20, and (d) year 130. The second row shows the corresponding generated velocity samples. The actual saturation model (third row) in (i) year 1, (j) year 5, (k) year 20, and (l) year 130. The fourth row shows the corresponding generated saturation samples.

of the  $\text{CO}_2$  plumes may not be accurately simulated over long periods of time (i.e., after year 20) because the physics knowledge becomes more limited with time.

Using the generated velocity models, we obtain synthetic  $\text{CO}_2$  saturation samples (Figures 9m-9p) via empirical relationships between saturation and velocity obtained from the well logs (Figure 10c). This procedure is illustrated for the injection well in year 20 in Figures 10a and 10b. Comparison with the actual values (Figures 9i-9l) proves that the synthetic saturation models obtained using the proposed method reflect the movement of the injected  $\text{CO}_2$  with sufficient accuracy.

Predictably, the results become less accurate with time (especially, after year 20) for the reasons listed below: 1. The  $\text{CO}_2$  plumes have similar contours in velocity and saturation. Hence, the synthetic saturation samples could not properly capture the plumes after year 20 because the corresponding velocity contours were inaccurate. 2. The high-saturation anomaly near the injection well is somewhat distorted because the velocity and  $\text{CO}_2$  saturation profiles from the well logs are not adequately represented by the linear fitting equations. 3. The simulated velocity distribution inside the  $\text{CO}_2$  plumes is homogeneous (i.e., it does not account for spatial variations), which reduces the accuracy of the synthetic saturation model.

Then the 28,000 synthetic data samples are randomly divided into the training (27,500) and validation (500) sets. After 140 epochs, the training loss flattens out at around 0.0013. Then, we test the trained neural network on the actual Kimberlina data that have the same acquisition geometry as the baseline survey. Note that the network employed in the hybrid strategy converges faster

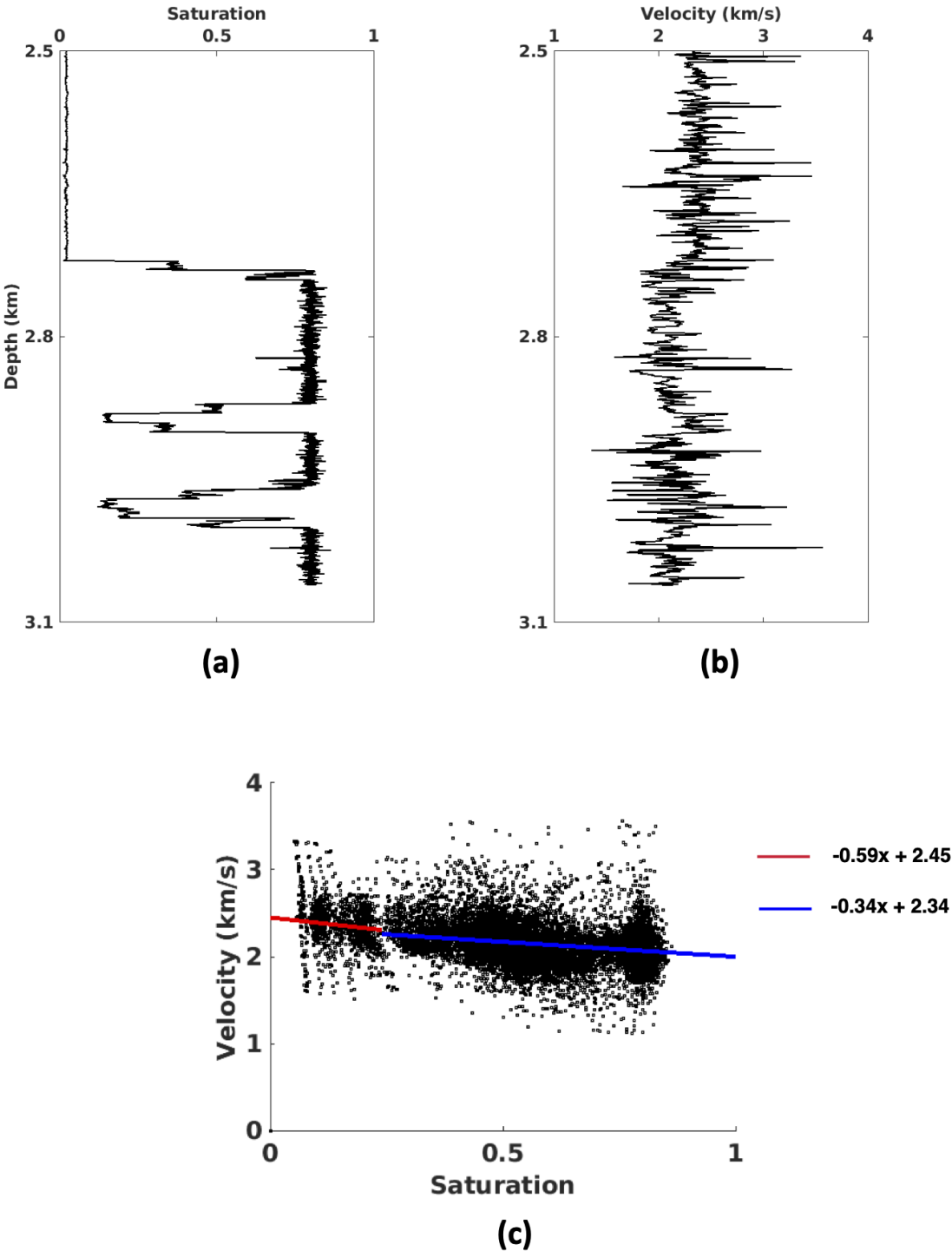


Figure 10. Well logs and empirical relationship between the velocity and CO<sub>2</sub> saturation for the injection well in year 20. The red and blue lines on plot (c) are two linear fitting equations separated according to the CO<sub>2</sub> saturation level.

	CPU/GPU	Number of (#) nodes	# Processors	# Training seismic surveys
Physics-based method	CPU	3	50	1
Hybrid	GPU	2	64	27,500
	# Iterations	Running time	Training time	Testing time per survey
Physics-based method	300	8.5 h	N/A	8.5 h
Hybrid	140	N/A	25.3 h	14 s

**Table 1.** Computational cost of the monitor inversion using the physics-based and hybrid strategies.

and produces a smaller loss than the pure data-driven method because of the higher quality of the training data. Both the velocity and saturation for the monitor survey in year 20 are well predicted by the trained neural network.

#### 4.4.1 Hybrid strategy vs. physics-based method

InvNet-VelSat can reconstruct the velocity (Figure 11c) and saturation (Figure 11f) from the monitor seismic data simultaneously and with sufficient resolution, which is not possible for the physics-based strategy. In general, our method outperforms the physics-based FWI (Figure 7f), which is confirmed by comparing the MAE values for the estimated velocity and by visually inspecting the results. The MAE for the velocity field reconstructed by our approach is 0.0084, whereas that of the physics-based method is 0.056. The CO<sub>2</sub> plumes and the high-velocity zone underneath are reconstructed with a higher resolution using the hybrid method (Figure 11c). However, the boundaries are positioned less accurately due to the limited physics information and simulation errors in the velocity-generation algorithm.

Because the baseline inversion is conducted by the physics-based FWI for both strategies, we compare the computational efficiency only for the monitor survey (Table 1). Although the training time of the hybrid approach (about 25.3 h) is significantly longer than the running time of the physics-based method (about 8.5 h), the testing (inversion) for one survey using the hybrid strategy takes only 14 s. Hence, the hybrid strategy is much more efficient than the physics-based method when processing multiple seismic surveys in real-time monitoring.

#### 4.4.2 Hybrid strategy vs. data-driven strategy

Compared to the velocity model predicted by the pure data-driven method (Figures 8b and 8c), the hybrid approach better captures the small “bump” and the low-velocity anomaly (Figures 11b and 11c). In addition, the hybrid algorithm (Figure 11c) succeeds in reconstructing the nonpermeable thin layers between the reservoirs without the false anomalies produced by the data-driven method (Figure 8c). These improvements are due to the more representative synthetic training data set generated using our method. Specifically, by leveraging a well-constrained background velocity distribution (the region outside the reservoir), the network can better capture essential geologic features from the training set and estimate the background velocity using the monitor surveys.

On the other hand, the hybrid strategy produces larger errors at the boundaries of the CO<sub>2</sub> plumes because of the inaccurate boundary delineation in the synthetic models (see above). Primarily due to the distortions at the boundaries, the overall MAE for the time-lapse velocity variations produced by our approach (0.0084) is larger than that of the data-driven method (0.0062).

Because the injected CO<sub>2</sub> is confined to the reservoir region, saturation outside the reservoir is supposed to vanish (Figure 6f), as correctly predicted by the hybrid method (Figure 11f). In contrast, the data-driven strategy yields nonzero saturation values (ranging between 0.02 and 0.06) in that area (Figure 8f). Although the contours of the plumes and the high-saturation zone near the injection well are not accurately estimated by the hybrid approach, its MAE for the entire saturation model (0.0075) is much smaller compared to that of the data-driven method (0.039).

We simulate the inverted/predicted baseline and monitor data and compute the time-lapse seismograms (Figure 12) by subtracting these two data sets. Compared to the actual record (Figure 12a), all three methods (Figure 12b-12d) produce artifacts near the first arrival due to the errors in the inverted time-lapse variations (Figures 7f, 8c, and 11c). In addition, because of the inaccurate parameter estimation outside the reservoirs, the physics-based FWI (Figure 12b) and data-driven method (Figure 12c) yield more intensive false reflection events after the first arrival than the hybrid approach. Hence, the proposed hybrid strategy outperforms the other two methods in the data domain.

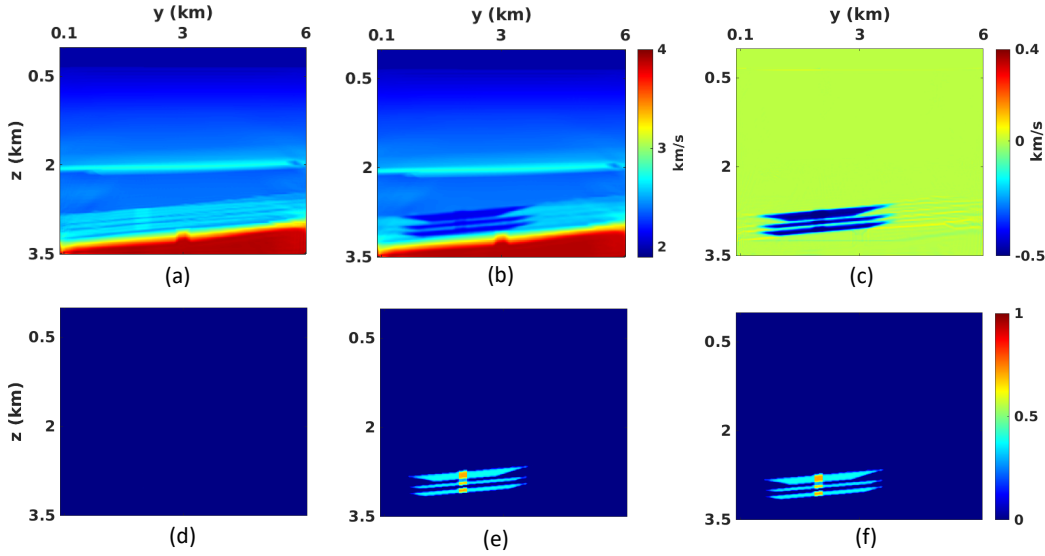


**Figure 11.** Baseline (a) velocity and (d) saturation models inverted by physics-based FWI. The monitor (b) velocity and (e) saturation models predicted by the hybrid time-lapse inversion. The time-lapse variations of (c) velocity and (f) saturation.

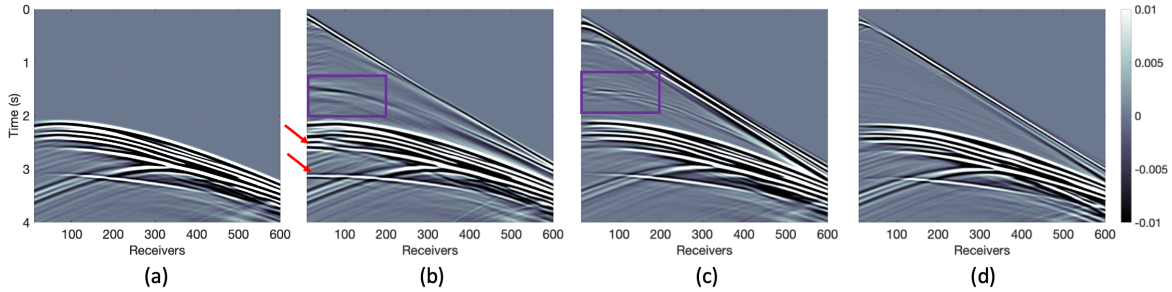


**Figure 12.** (a) Actual time-lapse seismogram (the difference between the monitor data in year 21 and baseline data in year 0). Time-lapse seismogram produced by (b) the physics-based FWI, (c) the data-driven method, and (d) the hybrid strategy. Artifacts after the first arrivals are either encircled in purple or marked by red arrows.

#### 4.5 Generalization and robustness: Hybrid strategy vs. data-driven strategy

Generalizability and robustness of a neural network indicate whether it is actually learning rather than simply memorizing the input-output relationship.

##### 4.5.1 Additional monitoring tests

To find out if the proposed hybrid approach is generalizable, we apply it to the remaining monitor surveys (not used in the training or validation). The three testing 2D monitor surveys (for years 1, 5, and 130) are acquired along the same line as the baseline survey. The testing is performed using InvNet-VelSat without any further fine-tuning. The velocity and saturation both inside and outside the three CO<sub>2</sub> plumes are reconstructed with sufficient accuracy (Figure 13). The differences between the actual and inverted temporal changes in all predicted monitor models are observed mostly at the boundaries. As expected, however, the prediction error increases with time.

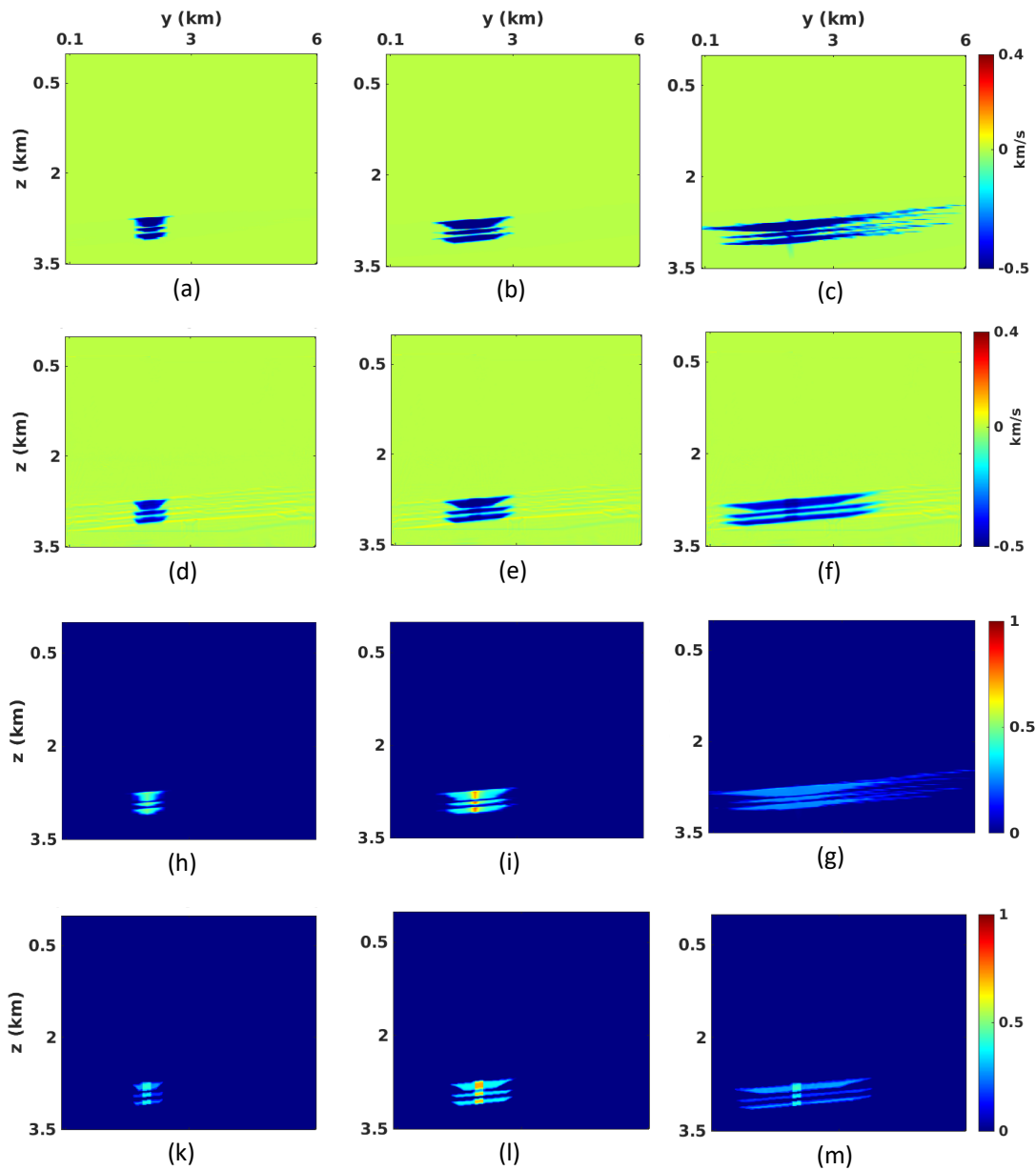


**Figure 13.** Actual time-lapse velocity variations for (a) year 1, (b) year 5, and (c) year 130. Plots (d), (e), and (f) show the predicted time-lapse velocity variations. The actual time-lapse saturation variations for (h) year 1, (i) year 5, and (g) year 130. Plots (k), (l), and (m) show the predicted time-lapse saturation variations.

#### 4.5.2 Influence of noise

Next, the testing monitor data for year 20 are contaminated with Gaussian noise that has the signal-to-noise ratio (SNR) equal to 10. The noise is added only to the testing data, whereas InvNet-VelSat is still trained on noise-free samples.

Predictably, both the data-driven and hybrid strategies produce more errors in the velocity and saturation changes estimated from the noise-contaminated data (Figure 14). For the velocity model obtained by the data-driven method, distortions are observed in the low-velocity layer above the CO<sub>2</sub> plumes (Zone 1), in the plumes themselves (Zone 2), and near the boundary between the reservoir and the deep high-velocity horizons (Zone 3). As a result, the corresponding MAE increases to 0.054, which is much larger than that for the noise-free data (0.0062).

In contrast, the hybrid strategy reconstructs Zones 1 and 3 with sufficient resolution, with the errors (MAE=0.013) mostly concentrated near the boundaries of the CO<sub>2</sub> plumes in Zone 2. Evidently, our method is more robust for noisy data than the

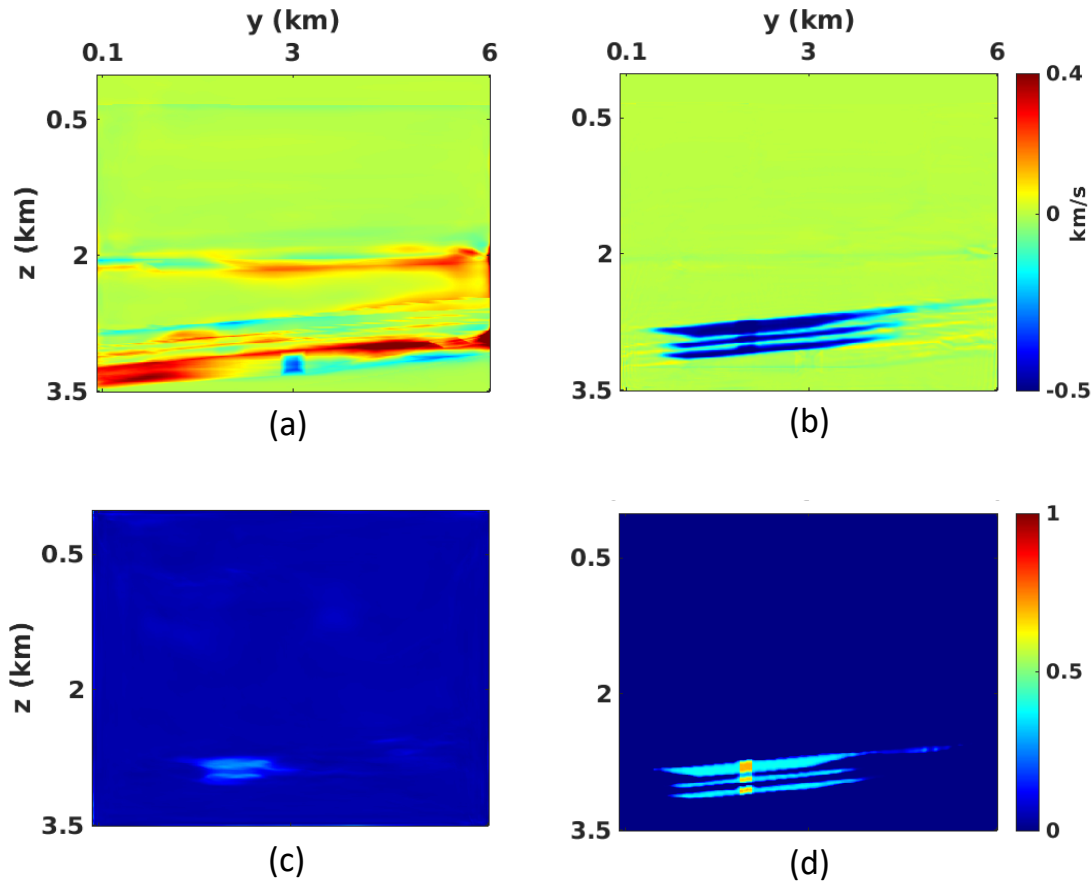


**Figure 14.** Temporal variations in the P-wave velocity obtained from noise-contaminated data (SNR = 10) by (a) the data-driven method and (b) the hybrid strategy. Plots (c) and (d) show the corresponding predicted time-lapse variations in the CO<sub>2</sub> saturation.

data-driven approach. Likewise, the hybrid strategy predicts the saturation from the noisy pressure recordings with higher accuracy (MAE=0.0085) than the data-driven method (MAE=0.043) by taking advantage of the large volume of high-quality training data.

## 5 CONCLUSIONS

We developed a time-lapse inversion workflow that does not require pre-existing training data by combining physics-based full-waveform inversion (FWI) and data-driven neural networks. First, FWI is applied to the baseline survey to estimate the background velocity model. Then data-driven inversion (InvNet-VelSat) is employed to predict the velocity and CO<sub>2</sub> saturation from the monitor data set. The training data for InvNet-VelSat are simulated with a data-generation method based on the reconstructed background velocity model and physics knowledge (i.e., well logs), which is expected to be available for typical CO<sub>2</sub>-sequestration projects. Because these training models are simulated using the inverted baseline data, the proposed workflow relies on the accuracy of the employed FWI algorithm.

The hybrid strategy is tested on realistic synthetic data from the Kimberlina reservoir. The training samples (i.e., the velocity and saturation models) simulated by our data-generation method adequately capture the spatial and temporal dynamics of CO<sub>2</sub> movement. The accuracy of the time-lapse variations predicted by the hybrid method is comparable to or even higher compared to the much more time-consuming physics-based FWI. Testing on noisy data for different time intervals illustrates the robustness and generalization capability of the hybrid strategy, whose performance is superior to that of the data-driven method. It should be emphasized that the hybrid strategy does not require a large volume of training data, which should facilitate its application to monitoring CO<sub>2</sub> sequestration.

**6 ACKNOWLEDGMENTS**

This work was funded by the U.S. Department of Energy (DOE) Office of Fossil Energy's Carbon Storage Research Program via the Science-Informed Machine Learning to Accelerate Real Time Decision Making for Carbon Storage (SMART-CS) Initiative, and also co-funded by the Laboratory Directed Research and Development (LDRD) Program under the project # 20210542MFR at Los Alamos National Laboratory. Y. Liu and I. Tsvankin will also acknowledge the support of the sponsors of the Center for Wave Phenomena (CWP) at Colorado School of Mines.

**REFERENCES**

- Ajo-Franklin, J., J. Peterson, J. Doetsch, and T. Daley, 2013, High-resolution characterization of a CO<sub>2</sub> plume using crosswell seismic tomography: Cranfield, MS, USA: *International Journal of Greenhouse Gas Control*, **18**, 497–509.
- Ali, A., and A. A. Al-Shuhail, 2018, Characterizing fluid contacts by joint inversion of seismic P-wave impedance and velocity: *Journal of Petroleum Exploration and Production Technology*, **8**, no. 1, 117–130.
- Alumbaugh, D., M. Commer, D. Crandall, E. Gasperikova, S. Feng, W. Harbert, Y. Li, Y. Lin, S. Manthila Samarasinghe, and X. Yang, 2021, Development of a multi-scale synthetic data set for the testing of subsurface CO<sub>2</sub> storage monitoring strategies: Presented at the American Geophysical Union (AGU 2021).
- ArayaPolo, M., J. Jennings, A. Adler, and T. Dahlke, 2017, Automated fault detection without seismic processing: *The Leading Edge*, **36**, no. 3, 208–214.
- Asnaashari, A., R. Brossier, S. Garambois, F. Audebert, P. Thore, and J. Virieux, 2012, Time-lapse imaging using regularized fwi: a robustness study: *SEG Technical Program Expanded Abstracts*, 1–5.
- , 2015, Time-lapse seismic imaging using regularized full-waveform inversion with a prior model: Which strategy?: *Geophysical Prospecting*, **63**, 78–98.
- Cao, J., and B. Roy, 2017, Time-lapse reservoir property change estimation from seismic using machine learning: *The Leading Edge*, **36**, no. 3, 234–238.
- Carcione, J., S. Picotti, D. Gei, and G. Rossi, 2006, Physics and seismic modeling for monitoring CO<sub>2</sub> storage: *Pure and Applied Geophysics*, **163**, 175–207.
- Dahlke, T., M. Araya-Polo, C. Zhang, C. Frogner, and T. Poggio, 2016, Predicting geological features in 3D seismic data: Presented at the 3D Deep Learning Workshop.
- Denli, H., and L. Huang, 2009, Double-difference elastic waveform tomography in the time domain: *SEG Technical Program Expanded Abstracts*, 2302–2306.
- Fabien-Ouellet, G., E. Gloaguen, and B. Giroux, 2017, Time domain viscoelastic full waveform inversion: *Geophysical Journal International*, **209**, 1718–1734.
- Feng, S., L. Fu, Z. Feng, and G. T. Schuster, 2021, Multiscale phase inversion for vertical transverse isotropic media: *Geophysical Prospecting*.
- Feng, S., and G. T. Schuster, 2019, Transmission+ reflection anisotropic wave-equation travelttime and waveform inversion: *Geophysical Prospecting*, **67**, 423–442.
- Furre, A. K., O. Eiken, H. Alnes, J. N. Vevatne, and A. F. Kiær, 2017, 20 Years of Monitoring CO<sub>2</sub>-injection at Sleipner: *Energy Procedia*, **114**, 3916–3926.
- Gassmann, F., 1951, *Über die Elastizität poröser Medien*: *Vierteljahrsschrift der Naturforschenden Gesellschaft in Zürich*, **96**, 1–23.
- Grana, D., and E. D. Rossa, 2010, Probabilistic petrophysical-properties estimation integrating statistical rock physics with seismic inversion: *Geophysics*, **75**, O21–O37.
- Hale, D., 2013, Methods to compute fault images, extract fault surfaces, and estimate fault throws from 3D seismic images: *Geophysics*, **78**, no. 2, 33–43.
- Hornik, K., M. Stinchcombe, and H. White, 1990, Universal approximation of an unknown mapping and its derivatives using multilayer feedforward networks: *Neural Networks*, **3**, 551–560.
- Huang, C., and T. Zhu, 2020, Towards real-time monitoring: data assimilated time-lapse full waveform inversion for seismic velocity and uncertainty estimation: *Geophysical Journal International*, **223**, 811–824.
- Kim, J., Z. Xue, and T. Matsuoka, 2010, Experimental Study on CO<sub>2</sub> Monitoring and Saturation with Combined P-wave Velocity and Resistivity: Presented at the SPE International Oil and Gas Conference, OnePetro.
- Li, Y., T. Alkhalifah, and Q. Guo, 2021, Target-oriented time-lapse waveform inversion using deep learning-assisted regularization: *Geophysics*, **86**, no. 4, R485–R495.

- Lin, Y., and L. Huang, 2015, Quantifying subsurface geophysical properties changes using double-difference seismic-waveform inversion with a modified total-variation regularization scheme: *Geophysical Journal International*, **203**, no. 3, 2125–2149.
- Liu, F., S. A. Morton, X. Ma, and S. Checkles, 2013, Some key factors for the successful application of full-waveform inversion: *The Leading Edge*, **32**, 1124–1129.
- Liu, Y., and I. Tsvankin, 2021, Methodology of time-lapse elastic full-waveform inversion for VTI media: *Journal of Seismic Exploration*, **30**, 257–270.
- , 2022, Source-independent time-lapse full-waveform inversion for anisotropic media: *Geophysics*, **87**, R111–R122.
- Lumley, D., 2010, 4D seismic monitoring of CO<sub>2</sub> sequestration: *The Leading Edge*, **29**, no. 2, 150–155.
- Mavko, G., and T. Mukerji, 1995, Seismic pore space compressibility and Gassmann's relation: *Geophysics*, **60**, no. 6, 1743–1749.
- , 1998, Bounds on low-frequency seismic velocities in partially saturated rocks: *Geophysics*, **63**, 918–924.
- Pevzner, R., M. Urosevic, D. Popik, V. Shulakova, K. Tertyshnikov, E. Caspari, J. Correa, T. Dance, A. Kepic, S. Glubokovskikh, S. Ziramov, B. Gurevich, R. Singh, M. Raab, M. Watson, T. Daley, M. Robertson, and B. Freifeld, 2017, 4D surface seismic tracks small supercritical CO<sub>2</sub> injection into the subsurface: CO<sub>2</sub>CRC Otway Project: *International Journal of Greenhouse Gas Control*, **63**, 150–157.
- Plessix, R.-E., S. Michelet, H. Rynja, H. Kuehl, C. Perkins, J. Maag, and P. Hatchell, 2010, Some 3D applications of full waveform inversion: EAGE Expanded Abstracts.
- Queiβer, M., and S. Singh, 2010, Time lapse seismic monitoring of CO<sub>2</sub> sequestration at Sleipner using time domain 2D full waveform inversion: SEG Technical Program Expanded Abstracts, 2875–2879.
- Queiβer, M., and S. C. Singh, 2013, Full waveform inversion in the time lapse mode applied to CO<sub>2</sub> storage at Sleipner: *Geophysical Prospecting*, **61**, 537–555.
- Raknes, E. B., W. Weibull, and B. Arntsen, 2015, Seismic imaging of the carbon dioxide gas cloud at Sleipner using 3D elastic time-lapse full waveform inversion: *International Journal of Greenhouse Gas Control*, **42**, 26–45.
- Renán, R.-G., J. Yang, Y. Lin, J. Theiler, and B. Wohlberg, 2022, Physics-consistent data-driven waveform inversion with adaptive data augmentation: *IEEE Geoscience and Remote Sensing Letters*, **19**, 1–5.
- Schmidt, M., 2005, Least squares optimization with L1-norm regularization: Technical report.
- Sigfusson, B., S. R. Gislason, J. M. Matter, M. Stute, E. Gunnlaugsson, I. Gunnarsson, E. S. Aradottir, H. Sigurdardottir, K. Mesfin, H. A. Alfredsson, D. Wolff-Boenisch, M. T. Arnarsson, and E. H. Oelkers, 2015, Solving the carbon-dioxide buoyancy challenge: The design and field testing of a dissolved co<sub>2</sub> injection system: *International Journal of Greenhouse Gas Control*, **37**, 213–219.
- Singh, S., I. Tsvankin, and E. Z. Naeini, 2020, Full-waveform inversion with borehole constraints for elastic VTI media: *Geophysics*, **85**, no. 6, R553–R563.
- Singh, S., I. Tsvankin, and E. Zahibi Naeini, 2018, Bayesian framework for elastic full-waveform inversion with facies information: *The Leading Edge*, **37**, 924–931.
- Tarantola, A., 1984, Linearized inversion of seismic reflection data: *Geophysical Prospecting*, **32**, 998–1015.
- U.S. Department of Energy, 2019, Science-informed machine learning for accelerating real-time decisions in subsurface applications (SMART) initiative.
- Vigh, D., K. Jiao, D. Watts, and D. Sun, 2014, Elastic full-waveform inversion application using multicomponent measurements of seismic data collection: *Geophysics*, **79**, no. 2, R63–R77.
- Virieux, J., and S. Operto, 2009, An overview of FWI in Exploration Geophysics: *Geophysics*, **74**, no. 6, WCC127–WCC152.
- Wagoner, J., 2009, 3D Geologic Modeling of the Southern San Joaquin Basin for the Westcarb Kimberlina Demonstration Project—A Status Report: Technical report.
- Watanabe, T., S. Shimizu, E. Asakawa, and T. Matsuoka, 2004, Differential waveform tomography for time-lapse crosswell seismic data with application to gas hydrate production monitoring: SEG Technical Program Expanded Abstracts, 2323–2326.
- Wu, Y., and Y. Lin, 2019, InversionNet: An efficient and accurate data-driven full waveform inversion: *IEEE Transactions on Computational Imaging*, **6**, 419–433.
- Xue, Z., J. W. Kim, S. Mito, K. Kitamura, and T. Matsuoka, 2009, Detecting and monitoring CO<sub>2</sub> with P-wave velocity and resistivity from both laboratory and field scales: Presented at the SPE International Conference on CO<sub>2</sub> Capture, Storage, and Utilization, OnePetro.
- Yang, Y., X. Zhang, Q. Guan, and Y. Lin, 2021, Making invisible visible: Data-driven seismic inversion with physics-informed data augmentation: *CoRR*, **abs/2106.11892**.
- Yuan, C., X. Zhang, X. Jia, and J. Zhang, 2019, Time-lapse velocity imaging via deep learning: *Geophysical Journal International*, **220**, no. 2, 1228–1241.

- Zhang, F., C. Juhlin, C. Cosma, A. Tryggvason, and R. G. Pratt, 2012, Cross-well seismic waveform tomography for monitoring CO<sub>2</sub> injection: a case study from the Ketzin Site, Germany: *Geophysical Journal International*, **189**, 629–646.
- Zhang, W., and J. Gao, 2021, Deep-learning full-waveform inversion using seismic migration images: *IEEE Transactions on Geoscience and Remote Sensing*, **60**, 1–18.
- Zhang, X., and J. Zhang, 2012, Edge preserving regularization for seismic traveltome tomography: *SEG Technical Program Expanded Abstracts*, 2830–2834.
- Zhang, Z., and T. Alkhalifah, 2020, High-resolution reservoir characterization using deep learning-aided elastic full-waveform inversion: The north sea field data example: *Geophysics*, **85**, no. 4, WA137–WA146.
- Zhang, Z., and Y. Lin, 2020, Data-Driven Seismic Waveform Inversion: A Study on the Robustness and Generalization: *IEEE Transactions on Geoscience and Remote Sensing*, **58**, 6900–6913.